


---

**Article:**
Ozdemir Kilinc, Z., Tyas, A. orcid.org/0000-0001-6078-5215, Goodall, R. et al. (1 more author) (2016) Energy absorption in lattice structures in dynamics: Nonlinear FE simulations. International Journal of Impact Engineering, 102. pp. 1-15. ISSN 0734-743X

https://doi.org/10.1016/j.ijimpeng.2016.11.016

---


# Energy absorption in lattice structures in dynamics: Nonlinear FE simulations

Zuhal Ozdemir, Andrew Tyas, Russell Goodall, Harm Askes

PII: S0734-743X(16)30281-0
DOI: 10.1016/j.ijimpeng.2016.11.016
Reference: IE 2783

To appear in: *International Journal of Impact Engineering*

Received date: 19 May 2016
Revised date: 3 November 2016
Accepted date: 26 November 2016

Please cite this article as: Zuhal Ozdemir, Andrew Tyas, Russell Goodall, Harm Askes, Energy absorption in lattice structures in dynamics: Nonlinear FE simulations, *International Journal of Impact Engineering* (2016), doi: 10.1016/j.ijimpeng.2016.11.016

**Highlights**

- A numerical analysis framework has been developed that captures the experimentally observed dynamic response of micro-lattices
- The framework has been demonstrated to be accurate and robust across two lattice geometries and two loading rates, with responses monitored at both the impact face and the distal face of the sample
- The results suggest that simple MDoF models can be developed to capture the response of such geometries under fast loading regimes

# Energy absorption in lattice structures in dynamics: Nonlinear FE simulations

Zuhal Ozdemir[a], Andrew Tyas[a], Russell Goodall[b], Harm Askes[a,**]

[a] *Department of Civil and Structural Engineering, The University of Sheffield*
[b] *Department of Materials Science and Engineering, The University of Sheffield*

**Abstract**

An experimental study of the stress-strain behaviour of titanium alloy (Ti6Al4V) lattice structures across a range of loading rates has been reported in a previous paper (Ozdemir et al., 2016). The present work develops simple numerical models of re-entrant and diamond lattice structures, for the first time, to accurately reproduce quasi-static and Hopkinson Pressure Bar (HPB) test results presented in the previous paper. Following the development of lattice models using implicit and explicit non-linear finite element (FE) codes, the numerical models are first validated against the experimental results and then utilised to explore further the phenomena associated with impact, the failure modes and strain-rate sensitivity of these materials. We have found that experimental results can be captured with good accuracy by using relatively simple numerical models with beam elements. Numerical HPB simulations demonstrate that intrinsic strain rate dependence of Ti6Al4V is not sufficient to explain the emergent rate dependence of the re-entrant cube samples. There is also evidence that, whilst re-entrant cube specimens made up of multiple layers of unit cells are load rate sensitive, the mechanical properties of individual lattice structure cell layers are relatively

*Corresponding author
**Tel. +44(0)114 222 5769; Fax: +44(0)114 222 5700
*Email address:* h.askes@sheffieldac.uk (Harm Askes)

insensitive to load rate. These results imply that a rate-independent load-deflection model of the unit cell layers could be used in a simple multi degree of freedom (MDoF) model to represent the impact behaviour of a multi-layer specimen and capture the microscopic rate dependence.

*Keywords:* lattice structures, impact and blast protection, finite element method (FEM), emergent rate-dependence

## 1. Introduction

Over the previous few decades, research into the quasi-static and dynamic behaviour and energy absorbing characteristics of cellular solids has been assessed using costly experiments, because of the extreme complexities associated with their collapse mechanisms. With the current advances in numerical methods, we can predict the response of cellular solids even under very highly nonlinear loading regimes with a reasonable accuracy. Thus, in recent years, numerical methods have been widely used for the characterisation of mechanical behaviour and energy absorption properties of cellular solids.

Numerical studies carried out on cellular solids are of both quasi-static and dynamic nature and have been performed on a wide range of materials including both stochastic (such as metallic foams) and periodic cellular solids (such as lattice structures, hallow rings). Aktay et al. (2008) studied the quasi-static crushing behaviour of honeycombs using detailed micro-mechanical models, homogenised modelling approach and a finite element-discrete particle model with semi-adaptive coupling (SAC) technique and compared the results of these models with experiments. The progressive

folding behaviour of square aluminium tubes subjected to quasi-static axial crushing was numerically investigated using FEM by El-Hage et al. (2005). Karagiozova et al. (2005) studied the dynamic response of circular and square aluminium alloy tubes subjected to an axial explosive load using experimental and numerical techniques. Particular attention was paid to the influence of the impulse and material properties on the energy absorption capacity of tubes. Compressive response of a multi-layered steel pyramidal lattice, which was investigated by underwater explosive tests, was simulated using a fully coupled Euler-Lagrange FE hydro code by (Wadley et al., 2008). Energy absorption, wave filtering and wave variation characteristics of ring systems after collapse were studied both experimentally and numerically by Wang et al. (2010). In the majority of the numerical studies, cellular structures are assumed to have perfect geometries. However, the extent of imperfections can be more easily considered and controlled in a numerical model than a physical test. The effects of cell shape and cell wall thickness imperfections on the dynamic crushing behaviour of honeycomb structures were studied using the FEM by Li et al. (2007). Ajdari et al. (2011) carried out a numerical study on 2D honeycomb structures in order to clarify the effect of deformation rate, defects and irregularity on the behaviour of cellular structures. However, validation of the numerical model was not presented in their paper.

Although there are several disadvantages associated with experiments (for instance cost, time and collection of limited information during a fast dynamic phenomenon), experimental works conducted on a range of cellular materials have highlighted important issues associated with energy

absorption mechanisms of such materials when subjected to high loading rates. For instance, Reid and Peng (1997) and Vural and Ravichandran (2003) carried out Hopkinson Pressure Bar (HPB) and Split Hopkinson Pressure Bar (SHPB) tests on wood samples, respectively. Reid and Peng (1997) reported localised deformation mechanism and enhancement of crushing strength of wood under dynamic loading conditions. Vural and Ravichandran (2003) computed specific energy dissipation capacity of balsa wood and they found that it was comparable with those of fiber-reinforced polymer composites. Quasi-static and dynamic response of rectangular arrays of thin-walled metal cylindrical tubes were examined experimentally by Shim and Stronge (1986) and Stronge and Shim (1987), respectively. It was observed that the response of a tightly-packed array of ductile, thin-walled tubes under quasi-static and dynamic conditions is governed by the packing arrangement. Similarly, experiments carried out on diamond and re-entrant cube lattices (Ozdemir et al., 2016) demonstrated that unit cell geometry controls the force-deformation response of such structures. Goldsmith and Sackman (1992) determined the energy dissipation characteristics of bare honeycombs and sandwich plates with honeycomb cores using a ballistic pendulum. Alghamdi (2001) presented a review on mechanical properties of materials and devices including tubes, sandwich plates and honeycomb cells for dissipating kinetic energy.

A thorough understanding of the dynamic behaviour of cellular solids is crucial for maximising the performance of such materials particularly under high loading rates. The response of cellular solids may show quite distinctive differences under quasi-static and dynamic loads, because of rate sensitiv-

ity. The mechanisms of rate sensitivity of cellular materials consist of the strain rate dependence of the parent material, the microinertia effects, the compression and flow of air trapped in cells, the shock wave generation, the effect of micro-structural geometry and the influence of intrinsic length scale of the material. Several experimental and numerical studies have been undertaken on cellular materials to highlight mechanisms causing rate sensitivity. Lee et al. (2006a) carried out a series of quasi-static compression, Kolsky bar (SHPB) and gas gun experiments (HPB) on a type of open-cell aluminium alloy foam and stainless steel woven textile core materials. While the peak stress of open-cell foams was deformation insensitive, the rate-sensitivity of the peak stress was observed in the textile cores. Differences in local strain fields were observed in both materials at intermediate strain rates ($230 - 330\,\mathrm{s}^{-1}$), when compared with quasi-static loading conditions. This was attributed to the microinertia effects for the case of foam materials. At very high strain rates, the shock wave propagation was observed in both materials. In a following study, Lee et al. (2006b) undertook similar physical tests on pyramidal truss cores made of 304 stainless steel to investigate deformation modes of such materials. In addition, non-linear FE simulations were performed to understand the roles of material strain rate hardening and microinertia on the quasi-static and dynamic response of sandwich panels with pyramidal truss cores. At intermediate strain rates, microinertia effects caused differences in force-deformation response and deformation mode of such materials when compared with quasi-static loading conditions. At larger deformations, in addition to micro-inertia, the material strain rate hardening contributed to changes in deformation mode and stress-

strain response. Liu et al. (2009) studied the dynamic crushing behaviour of 2D Voronoi honeycomb using FE method. Three different deformation modes were observed at different loading ranges. These are: (1) quasi-static homogeneous modes where crush bands are located randomly and the deformation is macroscopically uniform; (2) transition mode in which crush bands are mainly concentrated at the impact end rather than the support end; and (3) shock mode where crush bands sequentially propagate from impact end to the distal end. The changes in deformation mechanisms and stress-strain response of Voronoi honeycomb observed under high loading rates were attributed to inertia effects. Zhao and Gary (1998) performed quasi-static and SHPB tests on aluminium honeycombs in the in-plane and out-of-plane directions. While the in-plane crushing behaviour of the aluminium honeycomb was rate insensitive, significant differences between static and dynamic out-of-plane crushing behaviour of the honeycombs were observed due to structural effects. Barnes et al. (2014) used direct impact tests to evaluated shock-like response of an open cell aluminium foam by developing shock-impact speed Hugoniot relations. As an extension of this work, Gaitanaros and Kyriakides (2014) used FE analysis to replicate the experimentally observed dynamic crushing behaviour of the open cell aluminium foam by forming planar shocks. Zheng et al. (2014) examined the dynamic stress-strain states in a closed-cell foam under direct impact conditions by creating FE models of the foam using 3D Voronoi technique. Sun et al. (2016) obtained a linear relation between shock speed and impact speed and established a unique linear Hugoniot relation to characterise shock constitutive relation for a 2D virtual foam.

In this study, we aim to develop simple FE models of titanium alloy (Ti6Al4V) lattice structures to reproduce quasi-static and Hopkinson Pressure Bar (HPB) test results reported in a previous study (Ozdemir et al., 2016) with a reasonable accuracy. In the literature, existing numerical and experimental studies on lattice structures focus mainly on two geometries: body-centred cubic (BCC) and a similar structure with vertical pillars (BCC-Z) (McKown et al., 2008; Mines et al., 2013; Smith et al., 2013). To the best of our knowledge, this is the first research to numerically investigate the dynamic response of re-entrant and diamond lattices. Imperfections of the lattice structures have not been accounted for in the numerical models and perfect models of re-entrant cube and diamond lattices have been built. In addition, there are very limited studies in the literature, which validate numerical results against experiments for the dynamic response of cellular solids over all duration of impact event (Lee et al., 2006b) and existing studies mainly focus on a maximum value of a response parameter (such as maximum displacement). Following the development of numerical lattice models using implicit and explicit non-linear finite element (FE) codes, in this work, these models are validated against experimental results during all time history of the impact event. Finally, the numerical models are utilised to explore further the phenomena associated with impact, the failure modes and strain-rate sensitivity of these materials.

The outline of the present paper can be summarised as follows: In Section 2, a nonlinear FE procedure for the analysis of quasi-static and impact response of diamond and re-entrant cube lattice structures is discussed briefly. Next, stress-strain response and associated failure modes of lattices, which

were captured by quasi-static compression tests, are simulated using the nonlinear FEM in Section 3. The energy absorption characteristics of lattices under high deformation rates are examined numerically in Section 4 by taking into account the effect of unit-cell geometric configuration. Finally, the influence of strain rate sensitivity of Ti6Al4V and radial confinement on the impact response lattice samples is assessed in Sections 5 and 6, respectively.

## 2. Nonlinear FE modelling

In this work, two unit cell geometries are chosen to carry out numerical HPB impact simulations. The geometries are diamond (Figure 1(a)), where the struts are arranged similar to the interatomic bonds in the atomic lattice of diamond, and re-entrant cube (Figure 1(b)), a cube shape with all edges and diagonal struts across the faces bent towards the centre; were it not for the fact that the unit cells of the lattice are connected at the corners, this last structure would resemble the auxetic structure of Lakes and Park (1998). The repeating unit cell is kept as a 5 mm side length cube for both lattices. Square strut cross-section was chosen for the diamond lattices with diagonal length of 1.0 mm, whereas the strut diameter of the re-entrant cube is 0.48 mm.

For HPB impact tests, a steel bar projectile and a Nylon 66 impactor are used for low and high velocity loadings, respectively. The steel projectile has a diameter of 25 mm, a length of 250 mm and a mass of 963 g. The Nylon 66 projectiles have a diameter of 27 mm, a length of 31 mm and a mass of 19.3 g. Two testing configurations were considered for the HPB tests: In the first case, the specimen was placed on the impact face of the HPB and

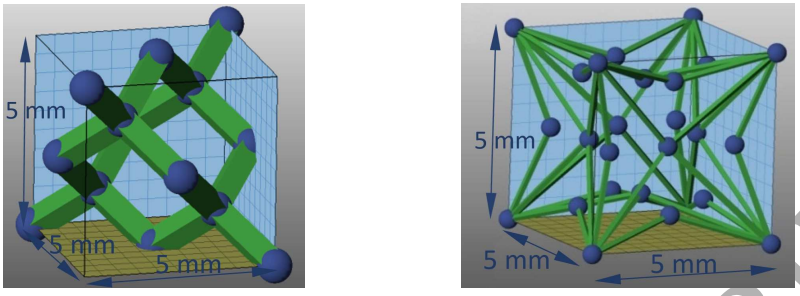


(a) (b)

Figure 1: Representative unit cells of (a) diamond and (b) re-entrant cube lattice structures.

the projectile was fired onto the specimen (Figure 2(a)). In the other case, the test specimens were fixed to the impact face of the projectile (Figure 2(b)). In these tests, 3D FE models of the impactor and HPB are built along with the full 3D models of lattices therefore, boundary conditions are taken care of by contact algorithms defined between the impactor and sample and between the HPB and sample. The HPB has a free boundary condition at its far end.

The multi-purpose nonlinear FE analysis program LS-DYNA is used to simulate the response mechanisms of lattice samples. Due to the fact that continuum elements are computationally expensive, 3D Timoshenko beam elements with plasticity and large deformation capabilities are used for the modelling of lattices. The main failure mechanisms of the lattices such as plasticity, buckling, and brittle shear failure are considered in the numerical model. In order to take into account plasticity, a material model pertaining to Von Mises yield condition with isotropic strain hardening is introduced in

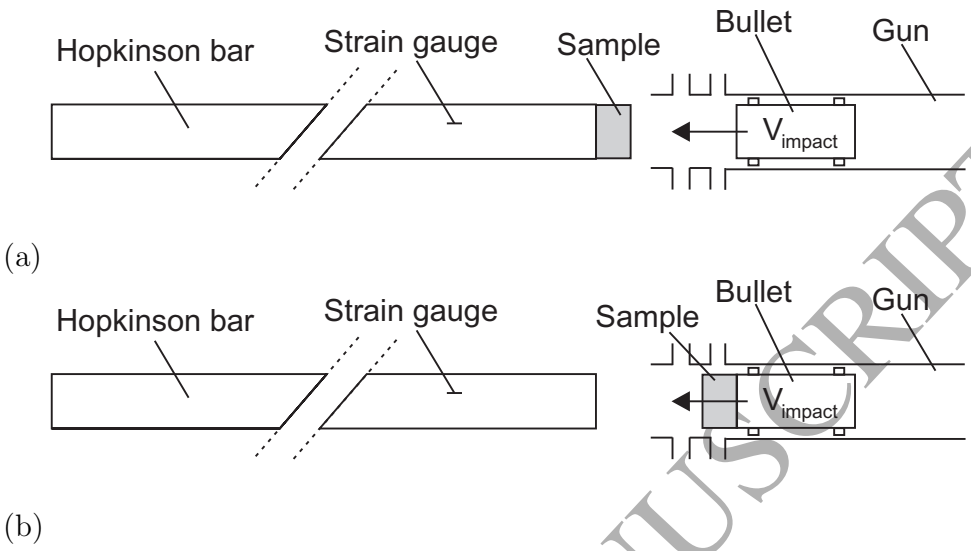


Figure 2: Two testing configurations for the HPB tests: (a) the distal face test and (b) impact face test.

the FE model. A plastic strain-based failure criteria, where the element is deleted when all the through thickness integration points reach the defined failure strain, is used in the model. Buckling is considered by activating geometric nonlinearity in the numerical simulations. In addition, struts are discretised by several beam elements in order to capture the micro-buckling of struts correctly. Tensile tests were performed on as-built round samples with a cross-sectional area of 24 $mm^2$ by following ASTM E8M-13a guidelines (E8M-13a (2013)) to determine mechanical properties of Ti6Al4V. In the material model, Ti6Al4V alloy is assumed to have a Young's modulus of 114 GPa, Poisson's ratio of 0.3, mass density of $4.43 \times 10^3\,kg/m^3$ and yield stress of 880 MPa. The values of these properties are also consistent with

the values obtained from the literature (Al-Bermani et al., 2010; Rafi et al., 2012). Numerical analyis results also indicated that the global response was not very sensitive to these particular values. Effective plastic strain to failure is set to be 0.3. Strain rate dependency of Ti6Al4V is ignored in the numerical simulations, unless otherwise stated. For the numerical quasi-static simulations, rigid material is assumed for the steel test rig. For the numerical HPB test simulations, a linear elastic material model with Young's modulus of 210 GPa, Poisson's ratio 0.3, mass density $7.80 \times 10^3$ kg/m$^3$ is assumed for the steel impactor. The Nylon 66 impactor is considered to exibit elastic-perfect plastic behaviour with Young's modulus of 1.7 GPa, Poisson's ratio of 0.4, mass density of $1.088 \times 10^3$ kg/m$^3$, yield stress of 160 MPa and tangent modulus of 1.00 MPa. All the input data for the material models used in the quasi-static and impact tests are given in Table 1 along with the LS-DYNA material number and name.

In the FE simulations, the interaction forces between parts are transferred with contact algorithms. The so-called one-way contact algorithm (*CONTACT_AUTOMATIC_NODES_TO_SURFACE), in which only slave nodes (lattice nodes) are checked for penetration of the master segments (test rig), is used to model the interaction between lattices and test rig in the numerical quasi-static simulations. The friction forces between the test rig and lattice sample are taken into account with static and dynamic friction coefficients of 0.1. For the numerical HPB test simulations, two separate one-way contact types (*CONTACT_AUTOMATIC_NODES_TO_SURFACE) are used to model the force transfer between the impactor and lattice sample and the interaction between the lattice sample and HPB. Self-contact of the

lattices is modelled using a beam-to-beam contact algorithm (*CONTACT _AUTOMATIC_GENERAL). Static and dynamic friction coefficients are defined as 0.30 for all contact cases. Following the development of the finite element model of lattices, a mesh sensitivity analysis was carried out to ensure that the results are not sensitive to the mesh size; it was found that five beam elements per strut resulted in effective convergence of the results. The finite element models of 5-layer auxetic and diamond samples consist of 24320 and 8320 beam elements respectively. The length of each beam element is 0.543 mm and 0.433 mm for auxetic and diamond lattices, respectively. The rigid quasi-static test rig was modelled using 5408 four-node shell elements.

The experimental load-time signals from the impact loading events were recorded by means of a single HPB, 25 mm diameter, 3.4 m length, with a perimeter-mounted axial strain gauge station set 250 mm from the impact face of the bar. The strain gauge station thus recorded a distorted version of the impact load, due to well-known dispersion effects. As discussed in (Ozdemir et al., 2016), the impact load-time signals typically included significant energy at frequencies above that which can currently be accommodated by standard frequency domain dispersion correction techniques (Tyas and Watson 2001). Therefore, in order to compare like with like, the numerical models of the impact events included explicit modelling of the full HPB in addition to the impactor and lattice specimen. In the model, the load signal dispersed as it travelled along the model of the HPB, before being recorded on the bar perimeter at the location of the strain gauge in the experimental work, 250 mm from the impact face of the bar (Figure 3). In all subsequent comparisons of the experimental and numerical stress-time histories in

| Part | LS-DYNA Material number [–] | LS-DYNA Material name [–] | $\rho$ [kg/m$^3$] | $E$ [GPa] | $\nu$ [–] | $\sigma_y$ [MPa] | $E_{tan}$ [MPa] |
|---|---|---|---|---|---|---|---|
| Compression test rig | *MAT_020 | *MAT_RIGID | 7850 | 210 | 0.3 | – | – |
| Steel impactor & HPB | *MAT_001 | *MAT_ELASTIC | 7850 | 210 | 0.3 | – | – |
| Nylon impactor | *MAT_003 | *MAT_PLASTIC_KINEMATIC | 1088 | 1.5 | 0.4 | 160 | 1 |
| Ti6Al4V | *MAT_024 | *MAT_PIECEWISE_LINEAR_PLASTICITY | 4456.4 | 113.76 | 0.3 | 895.6 | – |

Table 1: Input data for all materials used in the numerical analyses.

this paper, the results are those measured at the gauge position. The HPB was modelled using 491904 and 724680 eight-node hexahedral elements in low and high velocity impact simulations, respectively. The steel and nylon impactors were represented with 39424 and 13200 eight-node hexahedral elements, respectively.

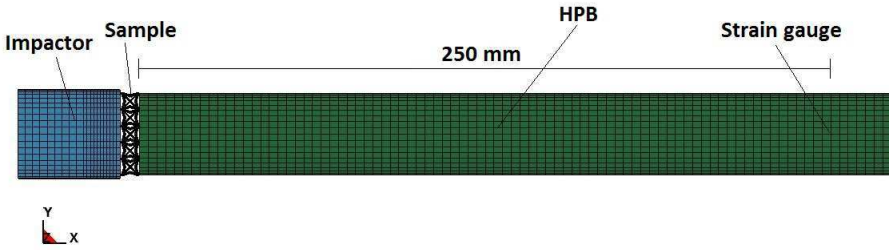


Figure 3: Schematic description of the 3D FE model of the HPB test setup

The average computation time for analysing low velocity impact tests of single and five-layer lattice samples was approximately 6 hours and 20 hours, respectively, on a quad core 64 bit PC with 2 GB memory. The finite element analysis of high velocity impact tests of single- and five-layer samples took around 40 minutes and 5 hours, respectively, on the same computer.

It is worth noting that stress measurements, whether experimental or numerical, may be influenced by edge (or size) effects in case of a low number cells in the height direction. Therefore, the findings of the experimental and numerical investigations regarding dynamic properties of lattices reported here are indicative only.

## 3. Nonlinear quasi-static behaviour of lattices

Single layer square samples of diamond and re-entrant cube lattices with an edge length of 25 mm and a height of 5 mm were compressed at a crosshead speed of 0.2 mm/min using a Hounsfield TX0038 universal test rig (Ozdemir et al., 2016). For each sample type, three quasi-static tests were carried out. The average stress-strain curves of the diamond and re-entrant cube samples following quasi-static compression tests are shown in Figures 4(a) and (b), respectively. As one can observe from these figures, the quasi-static stress-strain response of the re-entrant and diamond lattice structure show a typical of Type II (stretch dominated) response as defined by Ashby (2006), where a relatively constant initial stiffness is followed by post-peak softening, and later by final densification of the material.

Relative density $\bar{\rho}$, elastic modulus $E$, yield stress $\sigma_y$ and absorbed energy (up to densification) of the single-layer samples obtained following the quasi-static tests are summarized in Table 2. Strain limits up to 30 % and 60 % are chosen to compute absorbed energy for the re-entrant cube and diamond lattices, respectively. Stress-strain plots indicate that diamond lattices are more efficient than re-entrant cube trusses for energy absorption under quasi-static conditions, although the relative density of the re-entrant cube samples is higher than that of diamond lattices.

Numerical quasi-static stress-strain response of diamond and re-entrant cube lattices is also superimposed in Figures 4(a) and (b), respectively. An increase in initial stiffness of experimental stress-strain curves of re-entrant and diamond lattices at around of 80% and 180% is observed due to the initial crushing of diamond and re-entrant cube samples, respectively. Both

| Lattice structure | N. of layers | $\bar{\rho}$ [−] | $E$ [MPa] | $\sigma_y$ [MPa] | Absorbed energy [MJ/m$^3$] |
|---|---|---|---|---|---|
| Diamond | 1 | 0.137 | 132.2 | 11.8 | 2.32 |
| Re-entrant cube | 1 | 0.166 | 126.6 | 10.8 | 1.65 |

Table 2: Averaged material properties obtained following the quasi-static tests.

experimental and numerical stress-strain curves of diamond and re-entrant cube lattices show a clear peak load which coincides with the onset of fracture occurring in the struts near the nodes. After the peak load, post-yield softening behaviour is followed by a steep stress rise due to densification of the lattice layer.

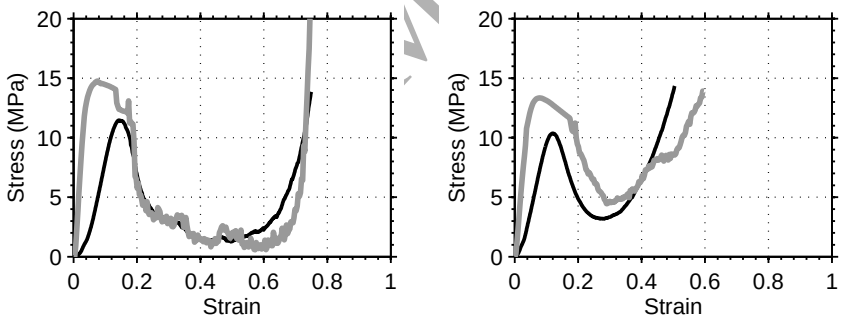


Figure 4: The average experimental (black line) and numerical (grey line) stress-strain curves of single-layer (a) diamond and (b) re-entrant cube samples obtained following the quasi-static compression tests.

An implicit time integration technique is employed to obtain economic

solutions for the quasi-static response of lattice structures. However, the implicit FEM encountered numerical difficulties when solving non-linear problem after the samples are compressed around 1 mm. Therefore, switching from the quasi-static implicit scheme to the dynamic explicit scheme with mass scaling is employed for both diamond and re-entrant cube lattice samples. The time step size is kept large enough to ensure that that kinetic energy is less than 5% of the peak internal energy. The numerical method predicts a higher initial stiffness than experiments for both re-entrant cube and diamond samples. In the numerical simulations, the geometry of the struts is assumed to be perfectly circular without any imperfection along their length. On the other hand, lattice struts manufactured by the Electron Beam Melting (EBM) technique include irregularities both in cross-section and along the length of the strut (Ozdemir et al., 2016) which act as weakeners. Therefore, the numerical method predicts somewhat higher strength and stiffness for the quasi-static response of diamond and re-entrant cube samples than is observed experimentally. Since the diameter of the struts in the diamond samples is larger than that of re-entrant cube samples, imperfections, which are independent of strut size, arising from the resolution limitations of the processing method, play a more important role in the quasi-static response of the re-entrant cube samples. A remarkable consistency of experimental and numerical deformed shapes of the re-entrant cube and diamond samples is observed following the quasi-static compression tests (Figure 5).

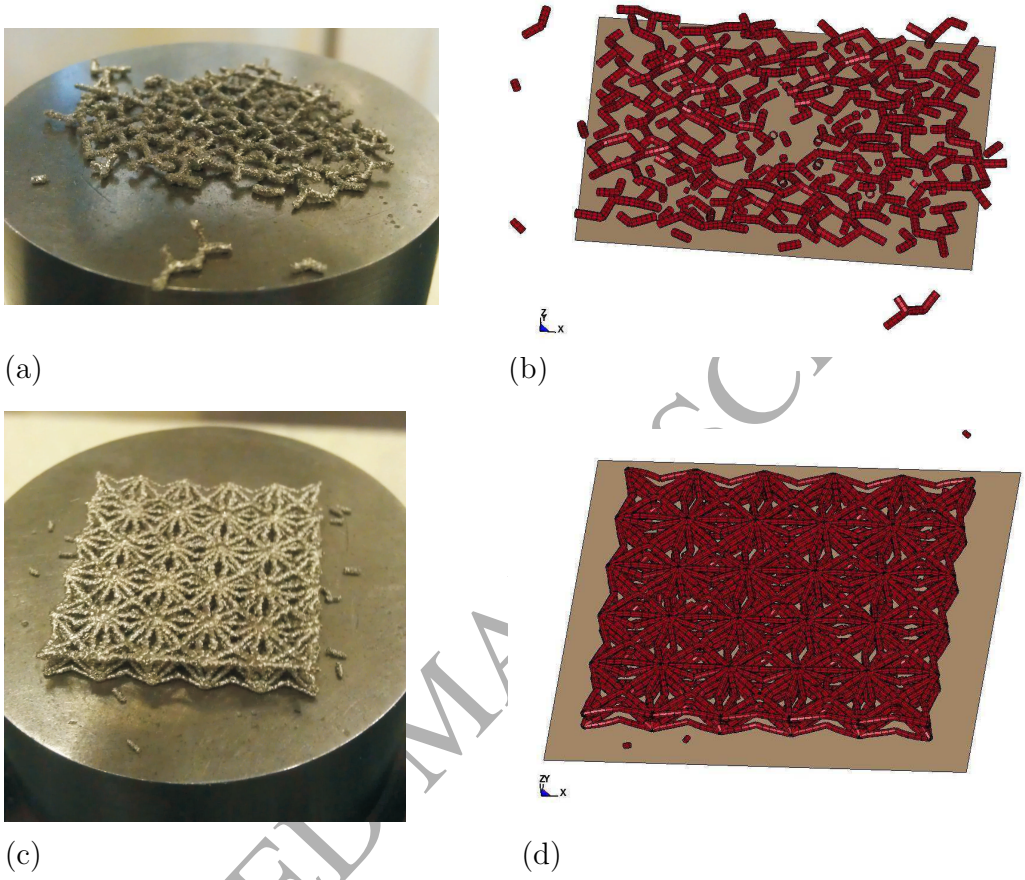


Figure 5: Deformed shape of diamond sample during quasi-static (a) experiment and (b) numerical simulation. Deformed shape of re-entrant cube sample during quasi-static (c) experiment and (d) numerical simulation. The pre-test sample sizes were 25 x 25 x 5 mm.

## 4. Nonlinear impact response of lattices

The HPB tests carried out with bare impactor and on single and multi-layer lattice samples are described in detail in (Ozdemir et al., 2016). In the present work, these test results are utilized to develop an effective modelling

tool using the FEM for the prediction of the mechanical behaviour, progressive damage and failure modes of the lattices. The same material models and material parameters defined in Section 3 are utilized in the numerical impact models as validated with quasi-static tests.

### *4.1. Impact tests with bare impactor*

Numerical simulations of low and high velocity impact tests were first carried out in the absence of the lattice specimen at the impact face of the HPB in order to verify the numerical models of the impactors. The steel and Nylon 66 impactors were fired at velocities of 7.6 m/s and 178 m/s during experiments, respectively, to transmit the same order of magnitude of impulse (around 6 Ns).

The experimental and numerical stress-time histories observed at the gauge station positioned 250 mm from the impact face of the HPB along with cumulative impulse-time histories are given in Figures 6 and 7. Although the numerical model predicts a higher peak stress than experiments for both low-velocity and high-velocity impacts, durations of the experimental and numerical main impact pulses are virtually the same. In experimental work, it is inevitable that a less-than-perfect alignment will be achieved between the impactor and the HPB. As a result, not all of the momentum of the impactor is transferred to the HPB in the first cycle of the stress wave through the length of the impactor. This results in an initial load plateau which is lower than would be assumed from 1-D theory and a subsequent low-magnitude coda to the main pulse which accounts for the majority of the residual impulse. These features are clearly seen on the experimental

stress-time history shown in Figure 6(a). On the other hand, the numerical model assumes that the impact surfaces of the impactor and the HPB are perfectly parallel, and as a result the coda is not observed in the numerical stress-time history. Impulse starts to increase when the impactor comes into contact with the HPB and remains unchanged following the rebound of the impactor (Figure 6(b)). Cumulative impulse-time histories suggest that rebound velocity of the impactors in the numerical simulation is higher than that observed in experiments.

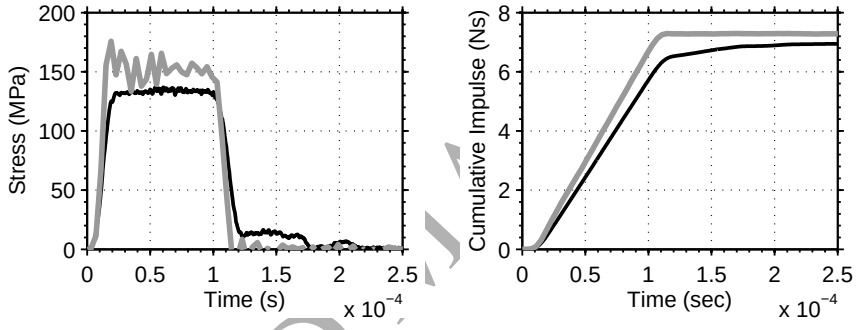


(a) (b)

Figure 6: Experimental (black line) and numerical (grey line) (a) stress and (b) cumulative impulse-time histories in the absence of lattice specimen generated by the steel impactor fired at a velocity of 7.6 m/s.

### *4.2. Impact response of single layer specimens*

Examples of experimental and numerical impact stress, cumulative impulse and strain time histories as well as stress-strain curves developed on the distal and impact face of single-layer re-entrant cube specimens induced

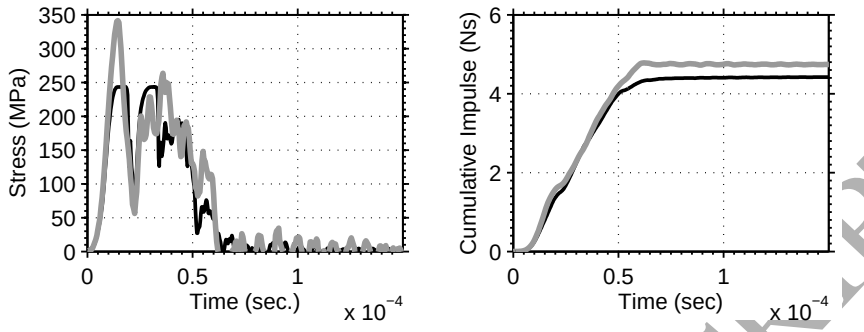


(a) (b)

Figure 7: Experimental (black line) and numerical (grey line) (a) stress and (b) cumulative impulse-time histories in the absence of lattice specimen generated by the Nylon 66 impactor fired at a velocity of 178 m/s.

by the steel impactor are shown in Figures 8 and 9, respectively. In these tests, the average strain rate is around $3700\,\mathrm{s}^{-1}$ and $3600\,\mathrm{s}^{-1}$, respectively. Figures 8(a) and 9(a) show examples of a good agreement between simulated and measured stress-time histories. Strain developed in the samples was not measured directly during the experiments. Therefore, the high speed video footage was used to estimate the displacement vs time record of the impacted face, from which the axial strain-time history was calculated. Subsequently, a stress-strain curve was derived for each test.

Numerical distal and impact face stress, cumulative impulse and strain time histories as well as stress-strain curves induced by the Nylon 66 impactor fired at velocities of 200 m/s and 187 m/s are shown in Figures 10 and 11, respectively. The average strain rate is around $42400\,\mathrm{s}^{-1}$ and $26000\,\mathrm{s}^{-1}$, respectively, in these tests. Experimental stress and cumulative impulse-time

histories are also superimposed in Figures 10(a), 10(b), 11(a) and 11(b). The resolution of the high speed video footage of high speed impact tests was not sufficient to estimate the displacement time histories of samples under high strain rates; strain vs time and stress vs strain curves for these samples could not be predicted. As one can observe from Figures 10(a), 10(b), 11(a) and 11(b), the stress and cumulative impulse-time histories obtained from experimental and numerical methods show a very good agreement for the first $5.5 \cdot 10^{-5}$ s. After $5.5 \cdot 10^{-5}$ s, the numerical results deviate from the experimental results. Comparison of the experimental and numerical cumulative impulse graphs given in Figures 10(b) and 11(b) shows that the numerical method predicts a higher rebound velocity for the Nylon 66 impactor than occurred in the experiment. This suggests that the difference between experimental and numerical stress-time histories for the high velocity impact tests (Figures 10(a) and 11(a)) is caused by the non-linear deformations of the Nylon 66 impactor, since an elastic-perfectly plastic material model for the impactor is used in the numerical simulations. Therefore, in reality, some part of the energy remaining in the system is dissipated by the fracture of the impactor, whereas, in the numerical models, this energy remains in the impactor and it rebounds with a higher velocity. This shows that we have captured the essentials in the stress-time lattice behaviour; late time differences caused by the fracture of the experimental impactor are of secondary importance and the lattice behaviour is modelled correctly.

The impact stress, cumulative impulse and strain time histories of two distal face impact tests (steel impactor at low speed, Nylon 66 impactor at high speed) differ significantly (Figures 12(a) - (c)). On the other hand, the

stress-strain curves of single-layer samples under low and high velocity loads strongly suggest that there is little difference in the distal face stress vs overall specimen strain at loading rates differing by an order of magnitude (Figure 12(d)). Therefore, we can conclude that distal face stress-strain response of single-layer re-entrant cube samples exhibits rate insensitive behaviour. Similar observations can be made for the impact stress, cumulative impulse and strain time histories of two impact face impact tests under low and high velocity loads (Figures 13(a) - (c)). However, the discrepancy between numerical stress vs strain curves under low and high velocity loads increases for impact face tests (Figure 13(d)).

### *4.3. Impact response of five-layer specimens*

Impact tests on five-layer lattice samples of the same diameter as the impactor were conducted to establish the ability of the lattices to extend the duration of the impact load and to reduce peak response (Ozdemir et al., 2016).

#### *4.3.1. Diamond lattices*

Examples of experimental and numerical distal face stress and cumulative impulse-time histories developed on the five-layer diamond lattices during low and high velocity impact tests are shown in Figures 14 and 15. In the case of the lower velocity impact, there is excellent correlation between the experimental and numerical results. The stress-time correlation is less good for the higher velocity impact, with the early time experimental stress being 10-15% higher than that predicted by the model, and the final peak associated

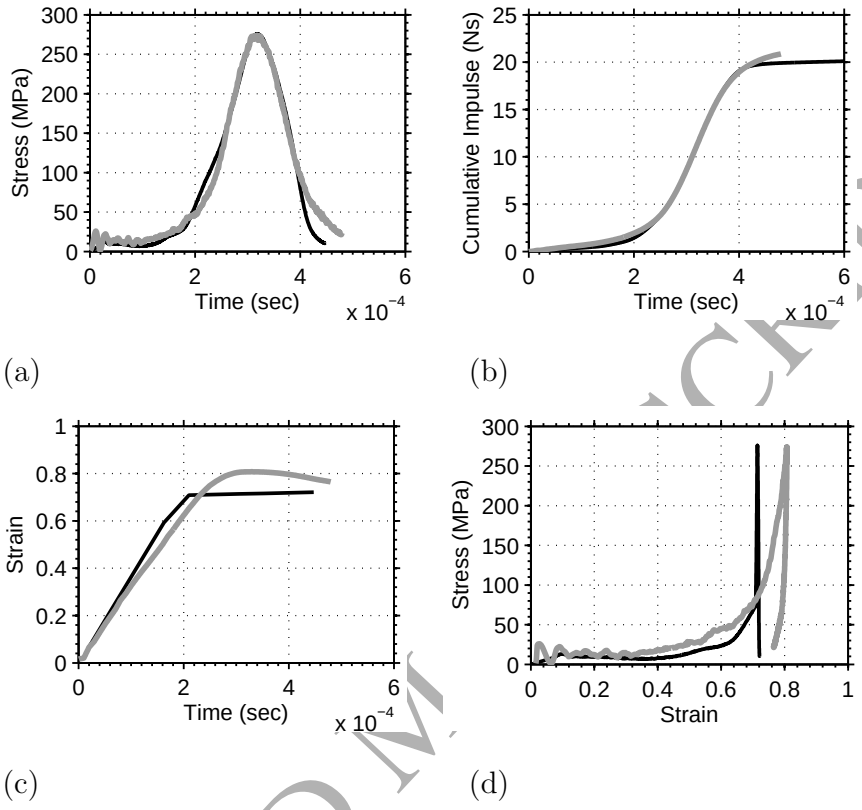


Figure 8: Experimental (black line) and numerical (grey line) distal face (a) stress, (b) cumulative impulse and (c) strain time histories, and (d) stress-strain curve of the single layer re-entrant cube lattice specimen induced by the steel impactor fired at a velocity of 18.8 m/s.

with full densification of the sample and final transfer of the residual momentum from the impactor being higher in the numerical model. However, the experimental and numerical final cumulative impulse results show good correspondence in both cases. This indicates that local fluctuations in the

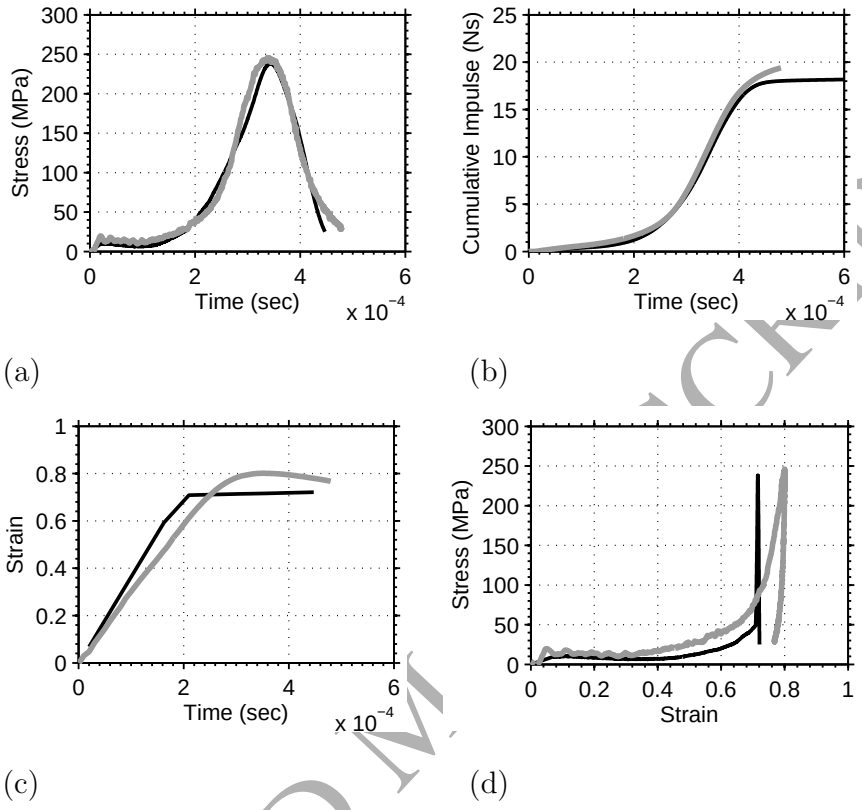


Figure 9: Experimental (black line) and numerical (grey line) impact face (a) stress, (b) cumulative impulse and (c) strain time histories, and (d) stress-strain curve of the single layer re-entrant cube lattice specimen induced by the steel impactor fired at a velocity of 17.7 m/s.

stress-time histories average themselves out.

Figure 16 shows numerical and experimental impact face stress vs time and cumulative impulse vs time plots of five-layer diamond lattice induced by the Nylon 66 projectile. The discrepancies between experimental and

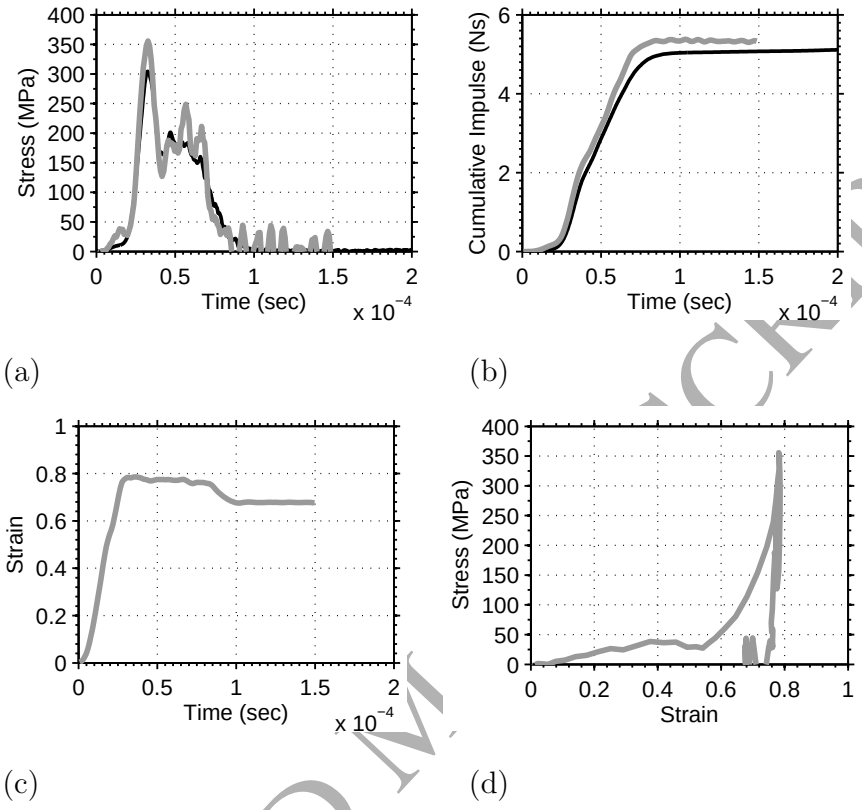


Figure 10: Experimental (black line) and numerical (grey line) distal face (a) stress, (b) cumulative impulse and (c) strain time histories, and (d) stress-strain curve of the single layer re-entrant cube lattice specimen induced by the Nylon 66 impactor fired at a velocity of 200 m/s.

numerical stress time histories can also be observed for impact face high velocity loads. However, the experimental and numerical cumulative impulse time histories show a good correlation for both cases.

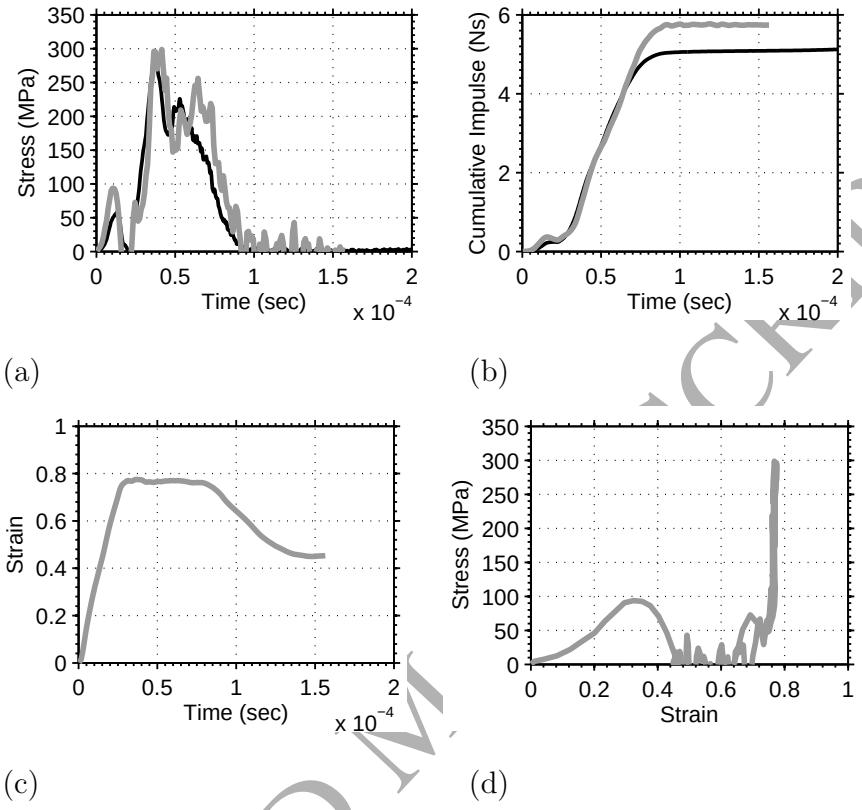


Figure 11: Experimental (black line) and numerical (grey line) impact face (a) stress, (b) cumulative impulse and (c) strain time histories, and (d) stress-strain curve of the single layer re-entrant cube lattice specimen induced by the Nylon 66 impactor fired at a velocity of 187 m/s.

*4.3.2. Re-entrant cube lattices*

Figures 17 -20 show numerical and experimental distal and impact face stress vs time and cumulative impulse vs time plots of five-layer re-entrant cube lattices induced by the steel and Nylon 66 projectiles. Numerical simu-

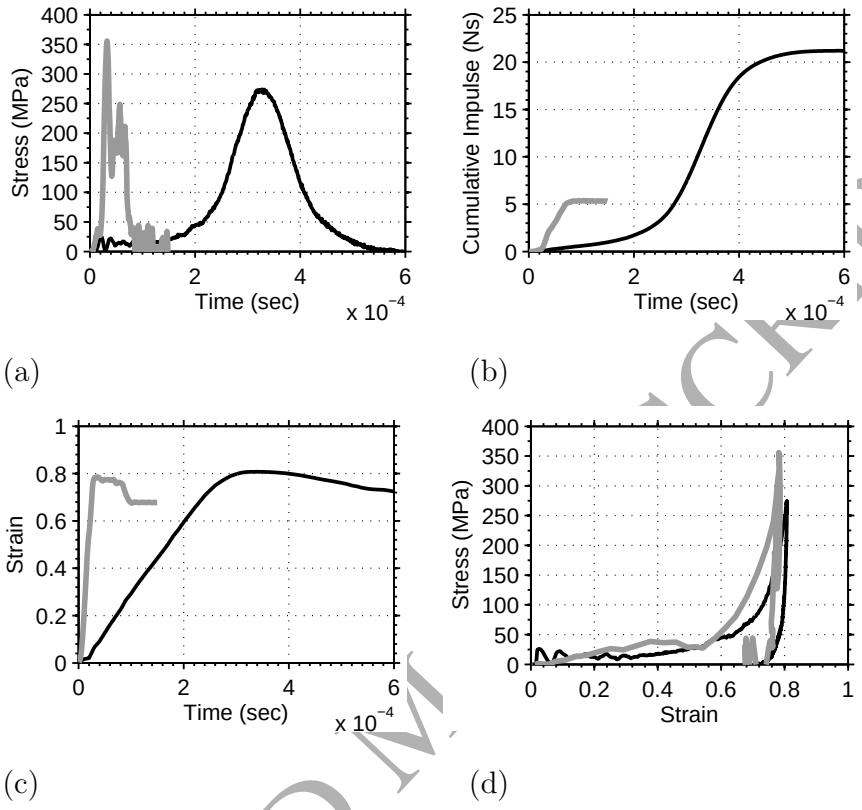


Figure 12: Numerical distal face (a) stress, (b) cumulative impulse and (c) strain time histories, and (d) stress-strain curves of the single layer re-entrant cube lattice specimens induced by the steel (black line) and Nylon 66 (grey line) impactors fired at velocities of 18.8 and 200 m/s, respectively.

lations can reasonably well predict the response of lattices under low velocity impact loads, while high frequency oscillations are observed both in the numerical plateau and the densification regime during high velocity impact tests, especially on the distal face.

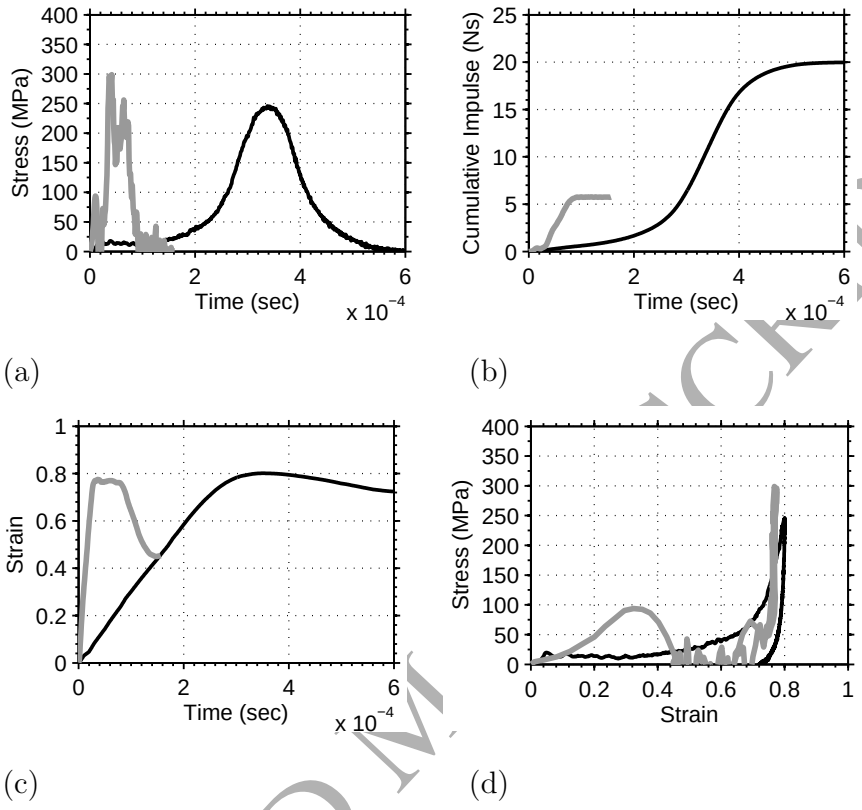


Figure 13: Numerical impact face (a) stress, (b) cumulative impulse and (c) strain time histories, and (d) stress-strain curves of the single layer re-entrant cube lattice specimens induced by the steel (black line) and Nylon 66 (grey line) impactors fired at velocities of 18.8 and 200 m/s, respectively.

As noted previously, the numerical model assumes perfectly co-axial and normal impact. This will inevitably lead to a faster rise time of the load, and hence, more significant high frequency content in the load-time signal. This may be the source of the high frequency oscillations in the early stages

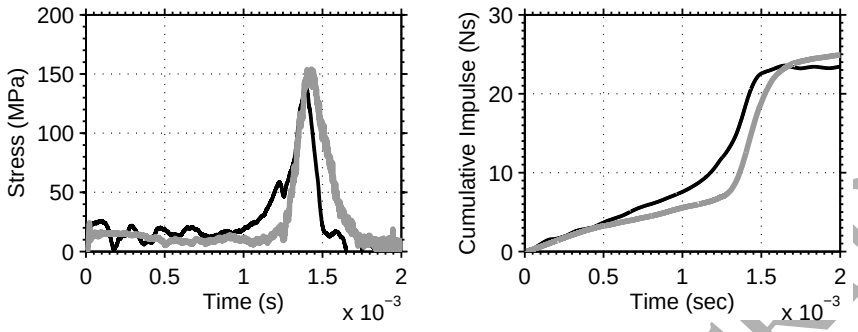


(a) (b)

Figure 14: Experimental (black line) and numerical (grey line) distal face (a) stress and (b) cumulative impulse-time histories of the five-layer diamond lattice specimen induced by the steel impactor fired at a velocity of 19.4 m/s.

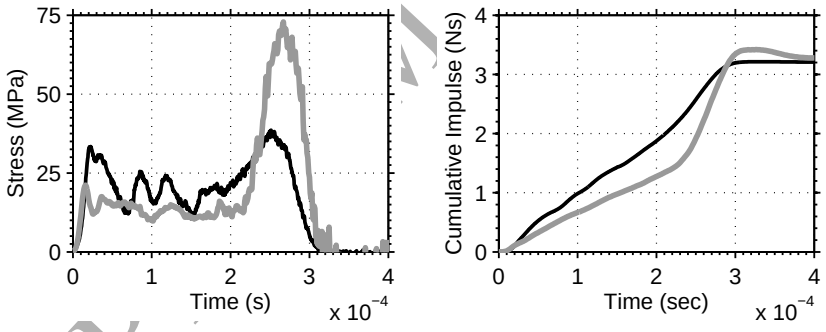


(a) (b)

Figure 15: Experimental (black line) and numerical (grey line) distal face (a) stress and (b) cumulative impulse-time histories of the five-layer diamond lattice specimen induced by the Nylon 66 impactor fired at a velocity of 140 m/s.

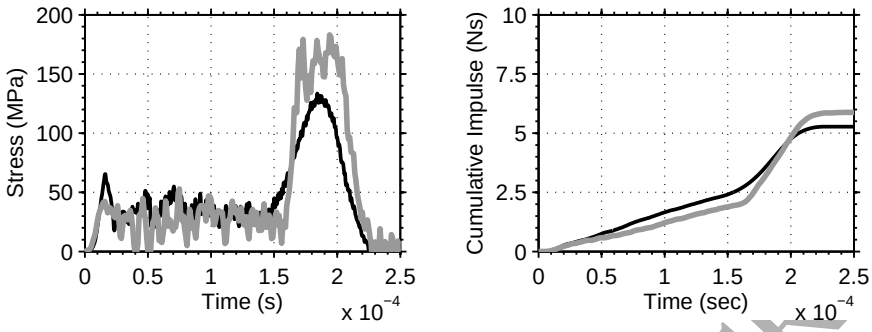


(a) (b)

Figure 16: Experimental (black line) and numerical (grey line) impact face (a) stress and (b) cumulative impulse-time histories of the five-layer diamond lattice specimen induced by the Nylon 66 impactor fired at a velocity of 165 m/s.

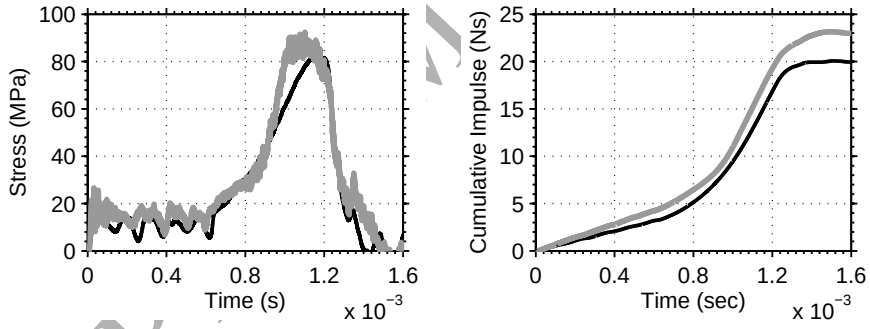


(a) (b)

Figure 17: Experimental (black line) and numerical (grey line) distal face (a) stress and (b) cumulative impulse-time histories of the five-layer re-entrant cube lattice specimen induced by the steel impactor fired at a velocity of 16.8 m/s.

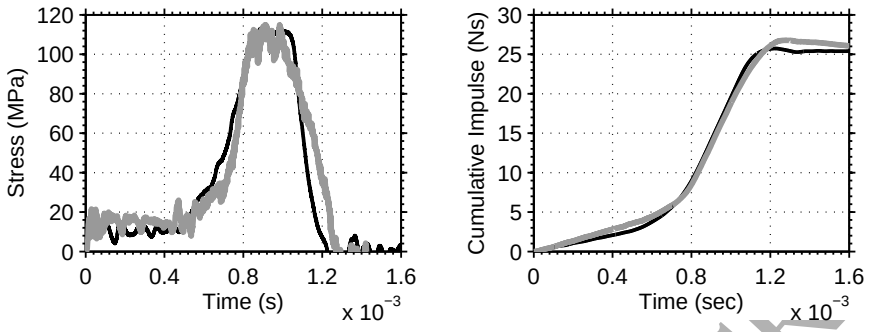


(a) (b)

Figure 18: Experimental (black line) and numerical (grey line) impact face (a) stress and (b) cumulative impulse-time histories of the five-layer re-entrant cube lattice specimen induced by the steel impactor fired at a velocity of 20.3 m/s.

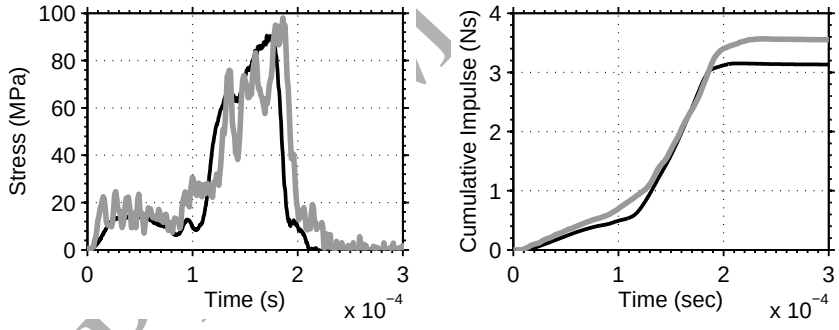


(a) (b)

Figure 19: Experimental (black line) and numerical (grey line) distal face (a) stress and (b) cumulative impulse-time histories of the five-layer re-entrant cube lattice specimen induced by the Nylon 66 impactor fired at a velocity of 134 m/s.

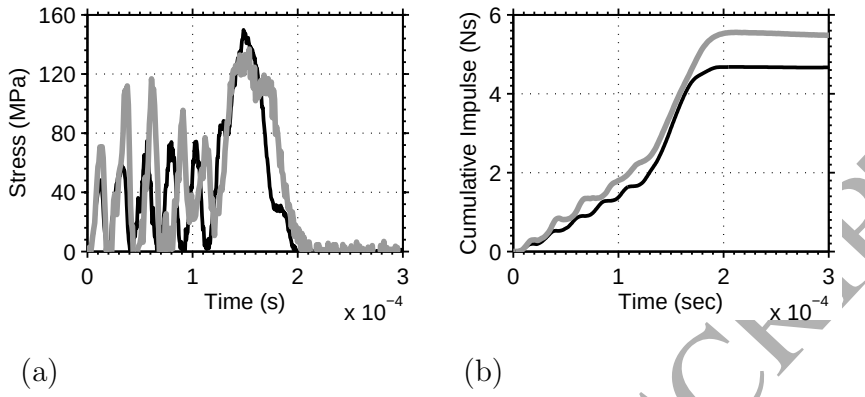


(a) (b)

Figure 20: Experimental (black line) and numerical (grey line) impact face (a) stress and (b) cumulative impulse-time histories of the five-layer re-entrant cube lattice specimen induced by the Nylon 66 impactor fired at a velocity of 136 m/s.

of the numerical signal in Figure 19(a). To assess the correlation between the experimental and numerical loads without this high frequency content, filtering was applied to the signals. An example of filtered experimental and numerical results using a low-pass filter with a cut-off frequency of 60000 Hz is shown in Figure 21, which is the filtered counterpart of Figure 19. The consistency of numerical and experimental results is improved by the elimination of very high frequency oscillations in the stress-time history. High frequency oscillations, which still exist in the numerical stress-time history after filtering, may be associated with the uncertainties in the material model of the Nylon 66 impactor.

In general, during impact tests, the specimen stress-time curve comprises a reasonably constant plateau load during cell collapse, followed by a much greater magnitude stress spike towards the end of the pulse (densification).

For low velocity impact tests, plateau load recorded during distal face and impact face tests have very similar values. However, for higher velocity impact tests, the impact face plateau stress is remarkably higher than distal face plateau stress. Similar observation was made by Liu et al. (2009) who reported the dynamic crushing behaviour of 2D Voronoi honeycombs at support and impact ends.

Both experiments and the FEM exhibit similar failure modes of re-entrant cube lattices for low and high velocity HPB tests. In the lower velocity (steel impactor) tests, the order of failure of the individual cell layers is random. This implies a slowly applied impact load is equilibrated along the entire length of the specimen and the order of cell layer collapse is governed by the strength discrepancies between layers due to the imperfect geometry of the struts along the length. Similar behaviour has been noted in the initial crushing of hexagonally-packed rectangular arrays of thin-walled metal tubes under quasi-static loads, which was localized in a narrow band (Shim and Stronge, 1986). The random location of this band was attributed to the local imperfections or weaknesses in the array. The higher velocity (Nylon 66 impactor) tests show that the failure of cell layers occurs sequentially from impact face to distal face as the deformation is localised. This indicates that equilibrium of load throughout the length of the specimen is not established at these higher velocities. This response is very similar to dynamic crushing behaviour of square-packed array in which propagates from the impact surface into the undeformed array. In hexagonally-packed arrays, dynamic crushing propagates from both the impact and distal ends (Stronge and Shim, 1987).

We have clear evidence of our layered system behaving as previous researchers have noted for other layered systems - layers failing in order of weakness at low impact velocities, layers failing in order of distance from impact face at high velocities as the deformation is localised (see for instance Figures 20 and 21 in (Ozdemir et al., 2016)).

Considering the difference in impact velocity from test to test, the impact and distal face stress-time histories from both the low-velocity and high-velocity impact tests demonstrate that diamond lattices appear to be marginally more efficient in temporally spreading the intensity of impact and reducing peak load than re-entrant cube lattices, even though re-entrant cube trusses have a higher relative density than diamond lattices.

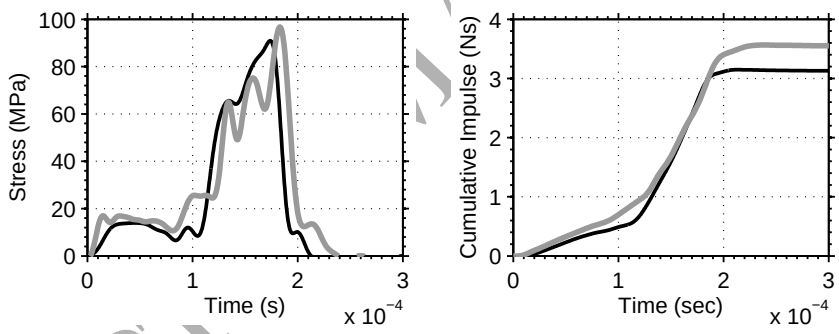


(a) (b)

Figure 21: Experimental (black line) and numerical (grey line) filtered distal face (a) stress and (b) cumulative impulse-time histories of the five-layer re-entrant cube lattice specimen induced by the Nylon 66 impactor fired at a velocity of 134 m/s.

## 5. Influence of intrinsic strain rate sensitivity of Ti6Al4V

In the previous numerical analyses, the intrinsic strain rate dependence of Ti6Al4V is ignored in the constitutive model. The Johnson-Cook material model captures strain hardening and strain rate sensitivity of a material by expressing stress as a function of strain and strain rate:

$$\sigma = (A + B\,\varepsilon^{n})\,\left(1 + C\ln\left(\frac{\dot{\varepsilon}}{\dot{\varepsilon}_{o}}\right)\right) \tag{1}$$

where $\sigma$ is the stress, $\varepsilon$ is the plastic strain, $\dot{\varepsilon}_{o}$ is a reference strain rate equal to 1 $s^{-1}$, $\dot{\varepsilon}$ is the effective plastic strain rate, $A$ is the yield stress, the combination of $B$ and $n$ governs the hardening behaviour of the material, and $C$ represents the strain rate sensitivity of the material. In this formulation temperature effects are ignored.

The influence of intrinsic rate dependency of Ti6Al4V on the impact response of single and multi-layer re-entrant cube lattice samples is assessed by using different $C$ values in the numerical simulations. A realistic value of strain rate sensitivity parameter $C$ for Ti6AL4V is reported to be on average 0.022 (Shao et al. (2010) and US-DOT-FAA (2000)). In addition to this realistic value, an extremely (and unrealistically) high value of $C = 0.1$ is also assumed and simulation results are compared with those of strain rate insensitive material model. Plots in Figure 22 show a comparison for distal face stress-time histories of the single and multi-layer re-entrant cube lattice specimens developed during low and high velocity impact tests. As can be seen from this figure, the realistic value of intrinsic strain rate sensitivity of the Ti6Al4V only very slightly affects the response of the single

and multi-layer re-entrant cube lattice samples. Even with such an unrealistically high value of $C = 0.1$, it is not possible to emulate the response of five-layer samples with a one-layer sample. This suggests that the rate-dependent behaviour that emerges at the macro-scopic level is *not* due to the rate-dependence of the Ti6Al4V alloy, but rather due to the interaction of stiffness and inertia at the unit cell level which can thus be adjusted and optimised according to user-defined performance requirements. The hypothesis regarding the source of rate-sensitivity of lattices needs further detailed investigations on numerical models of lattices in a future work. Liu et al. (2009) drawn similar conclusions in relation to the strain-rate sensitivity of 2D Voronoi honeycomb stating that the strain-rate sensitivity of cell wall material has minor effect on the dynamic response of such materials; rate effect is mainly caused by inertia. have also reached similar conclusions in their numerical study

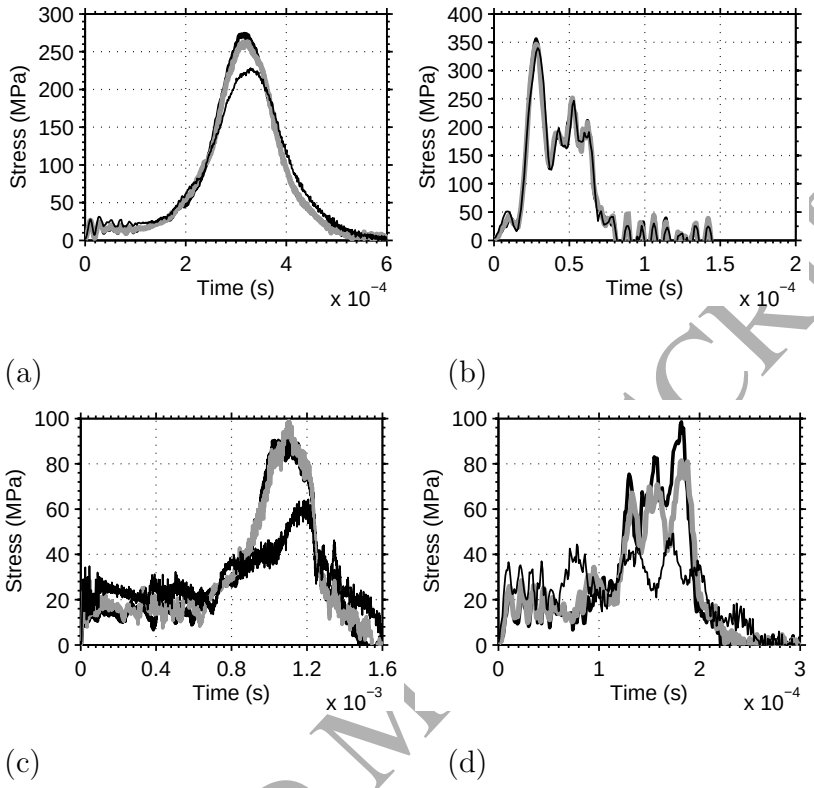


Figure 22: Distal face stress-time histories of (a) the single layer re-entrant cube lattice specimen induced by the steel impactor fired at a velocity of 18.8 m/s, (b) the single layer re-entrant cube lattice specimen induced by the Nylon 66 impactor fired at a velocity of 200 m/s, (c) the five-layer re-entrant cube lattice specimen induced by the steel impactor fired at a velocity of 16.8 m/s, and (d) the five-layer re-entrant cube lattice specimen induced by the Nylon 66 impactor fired at a velocity of 136 m/s for strain rate insensitive material model (thick black line), Johnson-Cook material model with C=0.02 (grey line) and C=0.1 (thin black line).

## 6. Effect of confinement

In the previous analyses, the impact behaviour of the lattice samples are numerically simulated under uniaxial loading conditions without radial constraint. Next, specimens are constrained against radial expansion by placing them inside a frictionless circular steel tube with a clearance fit, therefore, uniaxial straining of the samples is achieved. All other test parameters are the same as in Section 4. It is clear from Figure 23 that lateral confinement slightly affects the compressive response of re-entrant cube lattices for both low and high velocity impact tests. This is also consistent with the Poisson ratio of the re-entrant cube lattices which is near zero or negative (Almgren (1985)). The failure of the re-entrant lattice occurs in a systematic, layer-by-layer fashion, so confinement does not substantially affect the compressive stress of such lattices. However, a lattice specimen with a different mode of collapse should be assessed to quantify the influence of the confinement on the response of the structure.

Similar conclusions have been reached for different foam types under quasi-static conditions. Radford et al. (2005) evaluated the effect of lateral confinement on Alporas foam and only a small effect on the compression response was observed. This was attributed to the fact that the Alporas foam has a plastic Poisson ratio close to zero. Tan et al. (2005) radially confined Hydro/Cymat3 foam specimens and proposed that the radial confinement had little effect in the pre-densification regime.

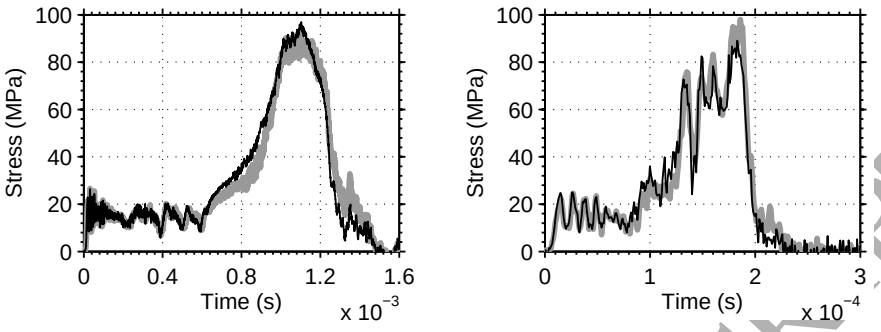


(a) (b)

Figure 23: Numerical unconfined (grey line) and confined (black line) distal face stress-time histories of five-layer re-entrant cube lattice specimens induced by (a) the steel impactor fired at a velocity of 16.8 m/s and (b) the Nylon 66 impactor fired at a velocity of 134 m/s.

## 7. Discussion

Numerical simulations carried out in this work demonstrate that the FEM is an efficient analysis tool for the prediction of the mechanical behaviour, progressive damage and failure modes of lattice materials. Considering disadvantages associated with continuum elements, 3D Timoshenko beam elements with appropriate contact properties were preferred for the modelling of lattice materials. Comparison of experimental and numerical results reveal that quasi-static and impact response of lattices with 3D Timoshenko beam elements is represented with high accuracy including individual collapse of cell layers and densification. This led to a drastic reduction in the total number of elements and degrees of freedom and, in turn, CPU time. On the other hand, practical design tools are vital for early stage of design due to the computational expense of the numerical methods. It is highly beneficial

to have a simplified model of lattice structures for generic assessment/design purposes in addition to a numerical tool.

A short review on the quasi-static deformation mechanisms of stretch dominated and bending dominated structures may help to explore the rate-sensitivity mechanism of lattices for future works . Most foams show a bending dominated behaviour, whereas lattice structures demonstrate a stretch dominated behaviour. Stiffnesses and initial collapse strengths of stretch dominated structures are higher than those of bending dominated structures of the same relative density, since the deformation mechanisms of stretch dominated structures are characterized by hard response modes like tension and compression rather than soft failure modes like bending. In stretch dominated response, initial yield of the material is followed by a post-yield softening stiffness caused by plastic buckling or brittle collapse of struts, whereas bending dominated structures continue to collapse at a nearly constant stress. Because of this, the energy absorption capacity of stretch dominated structures is less than that of bending dominated structures, although they are lighter Ashby (2006). Under dynamic loading, the collapse mode of cellular solids may change from a quasi-static failure mode to new mode involving additional stretching which can dissipate more energy. This phenomenon is called as micro-inertia which can cause an increase in the strength of cellular solids under dynamic loading conditions in addition to inertia and shock wave propagation effects Deshpande and Fleck (2000). Bending dominated structures are slightly affected by micro-inertia, strain-rate and inertia effects under dynamic conditions Calladine and English (1984).

Impact tests on single-layer re-entrant cube samples explained in Section

603 4.2 strongly suggest that the distal face stress-strain curves of single-layer re-
604 entrant cube samples exhibit little difference at loading rates even differing by
605 an order of magnitude (Figure 12(d)), while five-layer samples under low and
606 high velocity impact loads exhibit load rate sensitive behaviour (Figure 24).
607 These results imply that a rate-independent load-deflection model of the unit
608 cell re-entrant cube layers could be used in a simple multi degree of freedom
609 (MDoF) model of a multi-layer specimen to represent its impact behaviour.
610 A simple 1-D MDoF spring-mass model can therefore be developed, using
611 lumped masses representing the inertia of each unit cell layer. The stiffness
612 of each layer can be represented with a rate-independent stress-strain curve
613 based on the data in Figure 12(d).

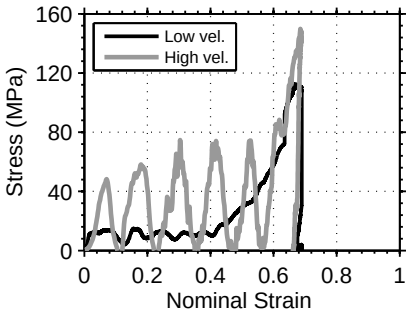


Figure 24: Numerical impact face stress-time histories of the five-layer re-entrant cube lattice specimen induced by the steel (black line) and Nylon 66 (grey line) impactors fired at velocities of 20.3 and 136 m/s, respectively

614 Regular periodic morphologies of lattice structures allow us to use such
615 simple spring mass systems for representing their impact response. There-
616 fore, we can specifically design 1-D layered systems for lattices to optimise

load spreading ability. However, the heterogeneous nature of foamed metals complicates the development of such simplified models for representing dynamic behaviour of metallic foams under high-strain rates. But, there will be certain restrictions in adopting an MDoF model: a physical justification for spring geometry can only follow from cell dimensions, and such a restrictive choice of parameters may limit the MDoF model's capability to provide the spatial resolution required for dynamic response capture.

A MDoF spring-mass model for multi-layer re-entrant cube samples is also consistent with the form of failure of such lattices. However, the efficiency of a similar MDoF system of another lattice type with a different mode of collapse should be elaborated carefully. In a future work, simplified design tools for lattices for impact threats will be studied in more detail. The relative accuracy by which multi-layer lattice structures can be modelled with a simple MDOF model raises the question to what extent the dynamic behaviour of lattice structures can be homogenised, and whether a homogenised model is able to capture the essential characteristics of localisation.

## 8. Conclusions

This work focuses, for the first time, on the development of simple FE models of diamond and re-entrant cube lattices for the characterisation of dynamic response of such materials. The FE models of lattices are built using 3D Timoshenko beam elements. The results of the previous extensive experimental study (Ozdemir et al., 2016) are utilized to collect more data on the quasi-static and impact behaviour of titanium alloy (Ti6Al4V) lattices. Numerical analysis results show that 3D Timoshenko beam elements with

appropriate contact properties are able to represent quasi-static and impact response of lattices with enough accuracy including individual collapse of cell layers and densification. Therefore, the FEM can be used an efficient tool for the prediction of the mechanical behaviour, progressive damage and failure modes of the lattice structures. Numerical impact analysis also reveals that intrinsic strain rate dependence of the Ti6Al4V cannot cause any emergent rate dependence of the response of the re-entrant cube lattices.

There is also some evidence that, whilst re-entrant cube specimens made up over multiple layers of unit cells are load rate sensitive, the mechanical properties of individual lattice cell layers are relatively insensitive to load rate. These results imply that a rate-independent load-deflection model of the unit cell layers could be used in a simple MDoF model of a multi-layer specimen to represent its impact behaviour. In a future contribution, we will focus on development of a simplified design tool of the lattices for impact threats. In addition, a more realistic material model will be used for Nylon 66 impactor and imperfections of lattices will be included in the numerical models in a future numerical modelling work.

## 9. Acknowledgements

Funding for part of this work was provided by the MOD's Armour and Protection Science and Technology Centre through project number DSTL-X1000054230. The authors would like to express their deepest gratitude to Mr Everth Hernandez-Nava and Professor Iain Todd for manufacturing lattice samples and conducting the quasi-static experiments in the Department of Material Sciences and Engineering of the University of Sheffield; and to

Mr Stephen Fay and Mr Alan Hindle for conducting the impact tests at the University of Sheffield Blast and Impact Laboratory, Buxton, UK.

## References

Ozdemir, Z., Hernandez-Nava, E., Tyas, A., Warren, J.A., Fay, S.D., Goodall, R., et al. Energy absorption in lattice structures in dynamics: Experiments. International Journal of Impact Engineering 2016;89:49–61.

Aktay, L., Johnson, A., B.H., K.. Numerical modelling of honeycomb core crush behaviour. Engineering Fracture Mechanics 2008;75(-):2616–2630.

El-Hage, H., Mallick, P., Zamani, N.. A numerical study on the quasi-static axial crush characteristics of square aluminium tubes with chamfering and other triggering mechanisms. International Journal of Crashworthiness 2005;10(-):183–196.

Karagiozova, D., Nurick, G., Chung Kim Yuen, S.. Energy absorption of aluminium alloy circular and square tubes under an axial explosive load. Thin-Walled Structures 2005;43(6):956–982.

Wadley, H., Dharmasen, K., Chen, Y., Dudt, P., Knight, D., Charette, R., et al. Compressive response of multilayered pyramidal lattices during underwater shock loading. International Journal of Impact Engineering 2008;35:1102–1114.

Wang, S., Zhao, K., Shen, J., Liu, K., Lu, G.. Dynamic process of ring systems as energy absorber subjected to lateral impact loading. International Journal of Crashworthiness 2010;15(6):605–615.

687 Li, K., Gao, X.L., Wang, J.. Dynamic crushing behavior of honeycomb
688 structures with irregular cell shapes and non-uniform cell wall thickness.
689 International Journal of Solids and Structures 2007;44:5003–5026.

690 Ajdari, A., Nayeb-Hashemi, H., Vaziri, A.. Dynamic crushing and energy
691 absorption of regular, irregular and functionally graded cellular structures.
692 International Journal of Solids and Structures 2011;48(3–4):506–516.

693 Reid, S., Peng, C.. Dynamic uniaxial crushing of wood. International
694 Journal of Impact Engineering 1997;19:531–570.

695 Vural, M., Ravichandran, G.. Dynamic response and energy dissipation
696 characteristics of balsa wood: experiment and analysis. International Jour-
697 nal of Solids and Structures 2003;40(9):2147–2170.

698 Shim, V.W., Stronge, W.. Lateral crushing in tightly packed arrays of
699 thin-walled metal tubes. International Journal of Mechanical Sciences
700 1986;28(10):709–728.

701 Stronge, W., Shim, V.W.. Dynamic crushing of a ductile cellular array.
702 International Journal of Mechanical Sciences 1987;29(6):381–406.

703 Goldsmith, W., Sackman, J.. An experimental study of energy absorption
704 in impact on sandwich plates. International Journal of Impact Engineering
705 1992;12(2):241–262.

706 Alghamdi, A.. Collapsible impact energy absorbers: An overview. Thin-
707 Walled Structures 2001;39:189–213.

Lee, S., Barthelat, F., Hutchinson, J., Espinosa, H.. Dynamic failure of metallic pyramidal truss core materials experiments and modelling. Int J of Plasticity 2006a;22:2118–2145.

Lee, S., Barthelat, F., Hutchinson, J., Espinosa, H.. Dynamic failure of metallic pyramidal truss core materials experiments and modeling. International Journal of Plasticity 2006b;22(-):2118–2145.

Liu, Y., Yu, J., Zheng, Z., Li, J.. A numerical study on the rate sensitivity of cellular metals. International Journal of Solids and Structures 2009;46(-):3988–3998.

Zhao, H., Gary, G.. Crushing behaviour of aluminium honeycombs under impact loading. International Journal of Impact Engineering 1998;21(-):827–836.

Barnes, A., Ravi-Chandar, K., Kyriakides, S., Gaitanaros, S.. Dynamic crushing of aluminum foams: Part i experiments. International Journal of Solids and Structures 2014;51:1631–1645.

Gaitanaros, S., Kyriakides, S.. Dynamic crushing of aluminum foams: Part ii analysis. International Journal of Solids and Structures 2014;51:1646–1661.

Zheng, Z., Wang, C., Yu, J., Reid, S., Harrigan, J.. Dynamic stressstrain states for metal foams using a 3d cellular model. Journal of the Mechanics and Physics of Solids 2014;72:93–114.

729 Sun, Y., Li, Q., McDonald, S., Withers, P.. Determination of the consti-
730 tutive relation and critical condition for the shock compression of cellular
731 solids. Mechanics of Materials 2016;99:26–36.

732 McKown, S., Shen, Y., Brookes, W., Sutcliffe, C., Cantwell, W., Langdon,
733 G., et al. The quasi-static and blast loading response of lattice structures.
734 Int Journal of Impact Engineering 2008;35(8):795–810.

735 Mines, R., Tsopanos, S., Shen, Y., Hasan, R., McKown, S.. Drop
736 weight impact behaviour of sandwich panels with metallic micro lattice
737 cores. International Journal of Impact Engineering 2013;60(-):120–132.

738 Smith, M., Guan, Z., Cantwell, W.. Finite element modelling of the
739 compressive response of lattice structures manufactured using the selec-
740 tive laser melting technique. International Journal of Mechanical Sciences
741 2013;67(-):28–41.

742 Lakes, , Park, J.. Negative poisson's ratio polymeric and metallic foams.
743 Journal of Materials Science 1998;23:4406–4414.

744 E8M-13a, A.I.. Standard Test Methods for Tension Testing of Metallic
745 Materials. 2013.

746 Al-Bermani, S., Blackmore, M., Zhang, W., Todd, I.. The origin
747 of microstructural diversity, texture, and mechanical properties in elec-
748 tron beam melted ti-6al-4v. Metallurgical and Materials Transactions A
749 2010;41(-):3422–3434.

750 Rafi, K., Karthik, N., Starr, T., Stucker, B.. Mechanical Property Evalua-
751 tion of Ti-6Al-4V Parts Made Using ElectronBeam Melting. Solid Freeform

752 Fabrication Symposium, SFF23, Laboratory for Freeform Fabrication at
753 The University of Texas at Austin; 2012.

754 Ashby, M.. The properties of foams and lattices. Philosophical Transactions
755 of the Royal Society A 2006;364:15–30.

756 Shao, F., Liu, Z., Wan, Y., Shi, Z.. Finite element simulation of machin-
757 ing of ti-6al-4v alloy with thermodynamical constitutive equation. The
758 International Journal of Advanced Manufacturing Technology 2010;49(65–
759 8):431–439.

760 US-DOT-FAA, . Experimental Investigations of Material Models for Ti-6Al-
761 4V Titanium and 2024-T3 Aluminum. US Department of Transportation
762 Federal Aviation Administration DOT/FAA/AR-00/25; 2000.

763 Almgren, R.. An isotropic three-dimensional structure with poisson's ratio
764 =-1. Journal of Elasticity 1985;15(4):427–430.

765 Radford, D., Deshpande, V., Fleck, N.. The use of metal foam projectiles
766 to simulate shock loading on a structure. International Journal of Impact
767 Engineering 2005;31:1152–1171.

768 Tan, P., Reid, S., Harrigan, J., Zou, Z., Li, S.. Dynamic compres-
769 sive strength properties of aluminium foams. part iexperimental data and
770 observations. Journal of the Mechanics and Physics of Solids 2005;53:2174–
771 2205.

772 Deshpande, V., Fleck, N.. High strain-rate compressive behaviour of
773 aluminium alloy foams. International Journal of Impact Engineering
774 2000;24:277–298.

775 Calladine, C., English, R.. Strain-rate and inertia effects in the collapse of
776 two types of energy-absorbing structure. International Journal of Mechan-
777 ical Sciences 1984;26(11).